

# Discovery of a pre-intermediate polar

David J. Wilson<sup>1</sup>★, Odette Toloza<sup>2</sup>, John D. Landstreet<sup>3,4</sup>, Boris T. Gänsicke<sup>2</sup>, Jeremy Drake<sup>5</sup>

<sup>1</sup> McDonald Observatory, University of Texas at Austin, 2515 Speedway, C1402, Austin, TX 78712, USA

<sup>2</sup> Department of Physics, University of Warwick, Coventry CV4 7AL, UK

<sup>3</sup> Armagh Observatory & Planetarium, Armagh, BT61 9DG, Northern Ireland, and

<sup>4</sup> Department of Physics & Astronomy, University of Western Ontario, London, ON N6G 1P7

<sup>5</sup> Center for Astrophysics | Harvard & Smithsonian, 60 Garden Street, Cambridge, MA 02138, USA

Accepted XXX. Received YYY; in original form ZZZ

## ABSTRACT

We present the discovery of a magnetic field on the white dwarf component of the detached, most common envelope binary CC Cet. Magnetic white dwarfs in detached binaries are extremely rare, in contrast to the high incidence of magnetism in single white dwarfs and cataclysmic variables. None of the proposed formation channels for magnetic white dwarfs can explain this discrepancy. We find Zeeman-split absorption lines in both ultraviolet *Hubble Space Telescope*/COS spectra and in optical VLT/UVES spectra of CC Cet. Model fits to the lines return a mean magnetic field strength of  $\langle |B| \rangle \approx 600\text{--}700\text{ kG}$ . Differences in the best fit magnetic field strength between observations and the high  $v \sin i$  of the lines indicate that the white dwarf is rapidly rotating with a magnetic field offset from the spin axis. The magnetic field strength and rotation period are consistent with the intermediate polar class of cataclysmic variables, and we compute stellar evolution models that predict CC Cet will evolve into an intermediate polar in 7–10 Myr. CC Cet is by far the hottest (and thus youngest) and has by far the weakest field of all magnetic white dwarfs in binaries known, and is so far separated from the rest of the sample that an alternative formation pathway may be required. In addition to the magnetic field measurements, we update the atmospheric parameters of the CC Cet white dwarf via model spectra fits to the COS data and provide a refined orbital period and ephemeris from *TESS* photometry.

**Key words:** binaries: close – stars: magnetic field – white dwarfs – stars: individual: CC Cet

## 1 INTRODUCTION

Post Common Envelope Binaries (PCEBs) are systems containing at least one evolved star, in which the initial separation was close enough that the secondary was engulfed by the expanding envelope of the primary as it passed through the giant stages of its evolution. After double-degenerates, the second most common type of PCEBs are white dwarfs plus main-sequence companions (Toonen et al. 2017). The vast majority of the known systems of this kind contain a white dwarf and an M-dwarf companion (Rebassa-Mansergas et al. 2010), though this is a selection effect as identification requires the white dwarf to be detectable against its main-sequence companion. For the remainder of this paper, we will use PCEB as synonymous for a close binary consisting of a white dwarf and a main sequence companion that formed through a common envelope. The common envelope dramatically shrinks the binary separation, leaving most PCEBs with orbital periods of  $\approx 0.1\text{--}5\text{ d}$  (Nebot Gómez-Morán et al. 2011). After emerging from

the common envelope, PCEBs lose angular momentum via gravitational radiation (Paczynski & Sienkiewicz 1981), and, if the main-sequence component possesses a convective envelope, magnetic wind braking (Rappaport et al. 1983). Consequently, the orbital separation decreases, eventually bringing the system into a semi-detached configuration, starting Roche-lobe overflow mass transfer from the companion onto the white dwarf – at this point, the PCEB will have evolved into a cataclysmic variable (CV).

Because these are stages along an evolutionary path, it could be expected that characteristics not affected by age or the mass transfer process should have the same distributions in both the PCEB and CV populations. This turns out not to be the case (distribution?). Most prominently, the occurrence rate of white dwarfs with detectable magnetic fields is hugely discrepant between the two populations (Liebert et al. 2005).

In a volume-limited sample of 42 CVs, Pala et al. (2020) found that  $36 \pm 7$  percent of the white dwarf primaries had magnetic field strengths  $\gtrsim 1\text{ MG}$ . Magnetic CVs are divided into polars with  $B \gtrsim 10\text{ MG}$ , where material from the secondary is accreted directly onto the poles of the white dwarf along the magnetic field lines, and intermediate polars with  $1 \lesssim B \lesssim 10\text{ MG}$ , in which an accretion disc

★ djwilson394@gmail.com

is formed but truncated at the magnetospheric radius. More complex structures such as rings and propellers can also be generated for certain combinations of magnetic field strength and white dwarf spin period (Norton et al. 2008). Whereas the spin periods of polars are locked to the binary period, the periods of intermediate polars are highly asynchronous, with some exhibiting spin periods of just a few tens of seconds (Lopes de Oliveira et al. 2020).

Very few robust measurements of the magnetic field strengths of white dwarfs in intermediate polars exist, as the white dwarf is typically outshone by the accretion flow, and the fields are too low to be detected via cyclotron emission from the accretion regions on the white dwarf. Variable polarised emission has been detected in a few intermediate polars (e.g. Potter & Buckley 2018), providing loose constraints on their magnetic fields strengths consistent with the expected  $1 \lesssim B \lesssim 10$  MG range.

In stark contrast to the CVs, magnetic white dwarfs in detached PCEBs are extremely rare. In a spectroscopic survey of over 1200 detached white dwarf plus M dwarf binaries, Silvestri et al. (2007) found just two candidate magnetic white dwarfs. Around ten pre-polars, magnetic PCEBs with fields  $> 10$  MG, are known (Schmidt et al. 2005, 2007; Schwöpe et al. 2009). In the intermediate polar range, SDSS J030308.35+005444.1 (Parsons et al. 2013) ( $B = 8$  MG) is the only unambiguous detection. A second, ambiguous case is the prototype PCEB V471 Tauri: A low S/N feature consistent with Zeeman splitting of the Si III 1207.5 Å by a  $\sim 350$  kG field was found by Sion et al. (1998), but extensive spectroscopic follow-up failed to detect Zeeman splitting at any other lines (Sion et al. 2012).

The rarity of magnetic white dwarfs in pre-CVs compared with their abundance in CVs could easily be explained if the magnetic field was induced by the mass transfer process after the system has become a CV. However, the proposed formation mechanisms for magnetic white dwarfs usually require the field to be generated either before or during the common envelope phase.

Several mechanisms have been suggested for field creation in white dwarfs. The fossil field hypothesis (Woltjer 1964; Angel et al. 1981; Braithwaite & Spruit 2004) suggests that the magnetic Ap and Bp stars represent the progenitors of magnetic white dwarfs, with their  $\sim$ kG strength fields enhanced to  $\sim$ MG fields by magnetic flux conservation as their radii shrink, although the space density of Ap/Bp stars is too low to account for all of the magnetic white dwarfs (Kawka & Vennes 2015). Alternatively the field may have been induced during the common envelope phase. Wickramasinghe et al. (2014) and Briggs et al. (2018) propose a model in which interactions between the two stars and the envelope induce strong differential rotation in the primary, generating a dynamo that enhances a preexisting weak field. The common envelope may end with the merger of the two objects, leaving an isolated magnetic white dwarf (Briggs et al. 2015), which would explain the higher average mass of magnetic white dwarfs compared with the population of non-magnetic white dwarfs (Ferrario et al. 2015). However Belloni & Schreiber (2020) found multiple issues with this pathway when compared with the observed population of PCEBs and CVs, in particular that the model produced too many magnetic white dwarfs, and that the predicted magnetic fields were too weak. However, the fossil field, common envelope and merger scenarios all imply that a white dwarf in a close binary emerges from the common envelope with its magnetic field in place, and therefore none of them explain the dearth of magnetic white dwarfs in detached binaries. Isern et al. (2017) propose instead that the white dwarf magnetic field is generated as a result of the crystallisation process as the white dwarf cools. This has the advantage of occurring well after

the common envelope, but it occurs too late to explain the magnetic CVs [numbers? Paper is unclear].

CC Cet (PG 0308+096) was identified as a post common envelope binary by Saffer et al. (1993) via radial velocity measurements of the H $\alpha$  line, with a  $\approx 6.9$  h period confirmed by Somers et al. (1996). The system consists of an unusually low-mass white dwarf ( $\approx 0.4 M_{\odot}$ ) and an M4.5–5 M dwarf secondary (Tappert et al. 2007). Here we present ultraviolet spectroscopy of the white dwarf component revealing Zeeman splitting induced by a  $6\text{--}700$  kG magnetic field, indicating that CC Cet is a low-mass pre-intermediate polar.

## 2 OBSERVATIONS

### 2.1 Hubble Space Telescope

CC Cet was observed with the Cosmic Origins Spectrograph (COS, Green et al. 2012) onboard the *Hubble Space Telescope* (HST) as part of program ID 15189. Observations were obtained on 2018 February 01 and 2018 July 22 with exposure times of 1865 s each, using the G130M grating with a central wavelength of 1291 Å. The spectra were reduced using the standard CalCOS tools. Figure 1 shows the spectrum from the first observation with the absorption lines discussed below marked. Due to the combination of the radial velocity shifts induced by the binary orbit and the magnetic splitting discussed below, we did not attempt to coadd the two spectra, instead analysing each one separately.

Of the other targets observed in program 15189, we use LM Com as a comparison star. LM Com was observed on 2017 December 17 with an exposure time of 1815 s and otherwise the same details as the CC Cet observations.

### 2.2 TESS

CC Cet was observed by the *Transiting Exoplanet Survey Satellite* (TESS, TIC 337219837) in Sector 4 (2018 October 19–2018 November 14) at 30 m cadence and again in Sector 31 (2020 October 12–2020 November 22), for which both 2 m and 20 s cadence data was returned (GO 3124, PI Hermes). Figure 2 shows the results of our analysis of the 20 m data using Lightcurve (Lightcurve Collaboration, 2018). The False Alarm Probability was calculated following the recipe from Bell et al. (2019). The light curve shows clear sinusoidal variation with a period of  $6.8818 \pm 0.00045$  h, in agreement with the orbital period of the binary system measured by Somers et al. (1996). The results from the 2 m data were double-checked against the 20 s data and a 30 m cadence light curve extracted from the Sector 4 data using the eleanor package (Feinstein et al. 2019). We find no evidence for additional variation modes with periods between 40 s and  $\approx 27$  d. A visual inspection of the 2 m light curve found no significant flare events.

### 2.3 XMM-Newton

We obtained X-ray measurements with the *XMM-Newton* (XMM) space telescope on 2018 July 22 for 16800 s, entirely overlapping the second HST observation.

### 2.4 VLT/UVES

CC Cet was observed with the Ultraviolet and Visual Echelle Spectrograph (UVES, Dekker et al. 2000) on the Very Large Telescope (VLT) as part of the Supernovae Type Ia Progenitor Survey (SPY,

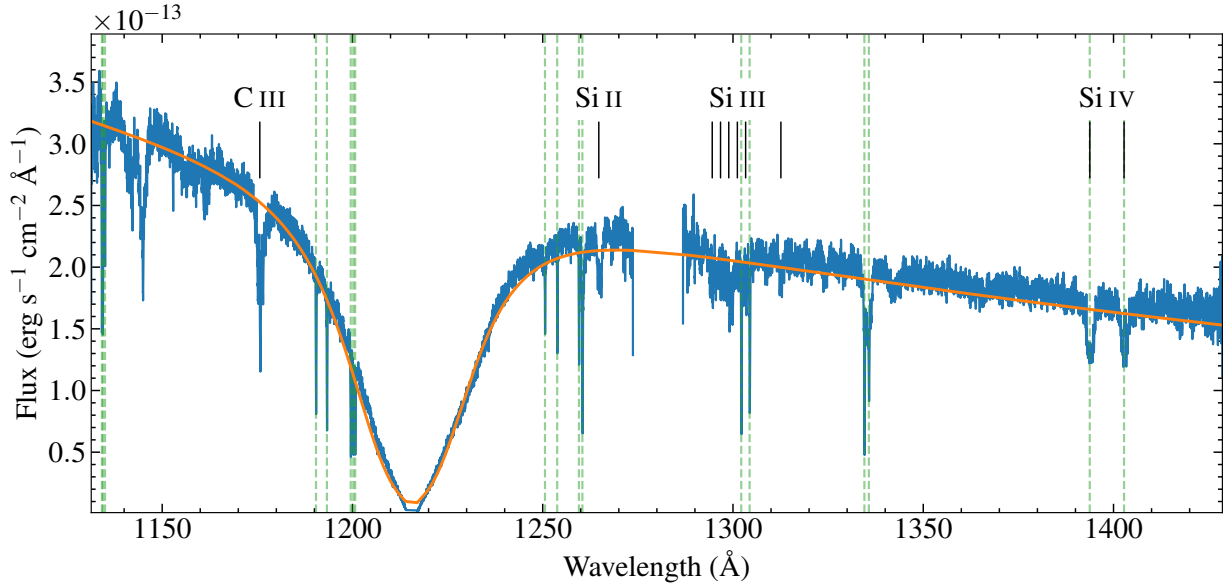


**Figure 1.** Full COS G130M spectrum of CC Cet obtained on 2018 February 01. The spectrum has been smoothed by a 5-point boxcar. The best fit model atmosphere spectrum is overplotted in orange. *[Redacted text]* Rest wavelengths of the C and Si absorption lines discussed in the text are labeled, and interstellar absorption lines are marked with green dashed lines.

Napiwotzki et al. 2020; Koester et al. 2009). The spectra were obtained on 2001 February 07–08 and cover the wavelength range 3281–6686 Å with  $R \approx 21000$ . We retrieved both spectra as fully calibrated data products from the ESO Archive Science Portal<sup>1</sup>.

### 3 MODELLING

#### 3.1 White dwarf characteristics

The two COS spectra of CC Cet show photospheric lines of Si IV, implying that the effective temperature ( $T_{\text{eff}}$ ) of the white dwarf is higher than 25000 K. To estimate *[Redacted]* of the atmospheric parameters of the white dwarf in CC Cet, i.e.  $T_{\text{eff}}$  and the surface gravity ( $\log g$ ) we fitted the continuum of the COS spectroscopy with synthetic models using the Markov Chain Monte Carlo (MCMC) technique. The Eddington flux ( $f_{\text{Edd}}$ ) of the models were scaled as,

$$F_{\text{obs}} = 4 \pi (R_{\text{wd}} \times \Pi)^2 \times f_{\text{Edd}}(T_{\text{eff}}, \log g), \quad (1)$$

where  $\Pi$  is the parallax and  $R_{\text{wd}}$  is the white dwarf radius.  $R_{\text{wd}}$  is a function of  $\log g$  and  $T_{\text{eff}}$  via the mass-radius relation for white dwarfs. We obtained the mass-radius relation for white dwarfs with hydrogen-rich atmospheres by interpolating the cooling models from Fontaine et al. (2001) with thick hydrogen layers of  $M_{\text{H}}/M_{\text{wd}} = 10^{-4}$ , which are available in the University of Montreal website<sup>2</sup>. In addition the models were corrected by reddening ( $E(B - V)$ ) using the extinction parameterization from Fitzpatrick (1999). In summary, the parameters to be fitted are:  $T_{\text{eff}}$ ,  $\log g$ ,  $D$ , and  $E(B - V)$ .

We set a flat prior on the parallax using the *Gaia* parallax for CC Cet ( $\Pi = 8.2381 \pm 0.0758$  mas, *Gaia* source id =

15207693216816512), which corresponds to a distance of  $D = 121.39 \pm 1.12$  pc, and force the fits to find the best parallax value within  $1\sigma$ . We set a Gaussian prior on the reddening of  $E(B - V) = 0.012 \pm 0.015$  mag based on the measurement from the STructuring by Inversion the Local Interstellar Medium (stilism)<sup>3</sup> at a distance of 120 pc. Regarding  $T_{\text{eff}}$  and  $\log g$ , we constrained their values within the limits of the grid of synthetic models for white dwarfs.

We used the grid of synthetic white dwarf models from (Koester 2010). The models have a pure hydrogen atmosphere (the parameter for mixing length convection was set to 0.8). They have effective temperature coverage of  $T_{\text{eff}} = 10000 - 35000$  K in steps of 200 K, and surface gravity in the range of  $\log g = -7.0 - 9.0$  dex in step of 0.1 dex.

The Earth airglow emission lines and the absorption lines of interstellar medium (see Table 1) and those of the white dwarf photosphere were masked out during the process (see Figure 1).

We used the python-based emcee MCMC method (Foreman-Mackey et al. 2013), where 100 walkers were sampling the parameter space during 10000 iterations. The likelihood function was defined as  $-0.5\chi^2$ . In general the walkers converged quickly, therefore we removed the first 250 steps from the chain. The samples of  $T_{\text{eff}}$ ,  $\log g$ , and  $E(B - V)$  follow a Normal distribution, except the samples of the parallax which clustered towards the lower tail of the distribution. While the parallax during the fits was tightly constrained to be within  $\pm 1\sigma$  from the *Gaia* average value, the fit hints that higher distances are required to get improve the far-ultraviolet spectroscopic fits of CC-Cet. For the normal distribution, we considered the median as the best value and the 15.9<sup>th</sup> and 84.1<sup>th</sup> percentiles for one standard deviation as error. The intrinsic uncertainties from the MCMC method are very small and they are purely statistical. The results are  $T_{\text{eff}} = 25245_{-19}^{+18}$  K,  $\log g = 7.606_{-0.004}^{+0.005}$  dex,  $E(B - V) =$

<sup>1</sup> <http://archive.eso.org/scienceportal/home>

<sup>2</sup> <http://www.astro.umontreal.ca/bergeron/CoolingModels>

<sup>3</sup> <https://stilism.obspm.fr/>

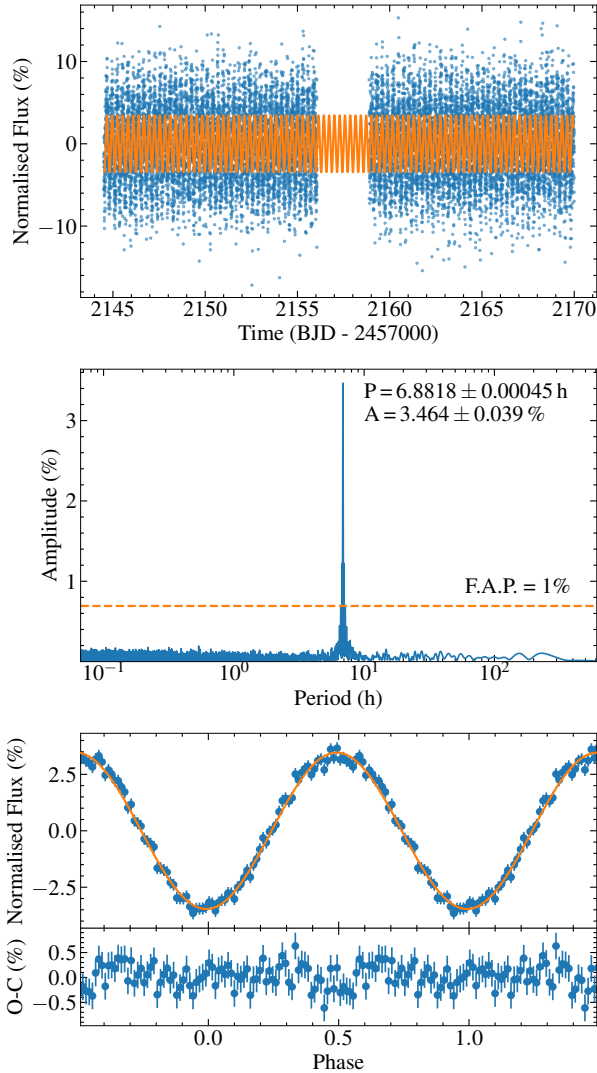


**Figure 2.** Top panel: *TESS* photometry of CC Cet with 2 m cadence (blue), with a model fit in orange. Middle panel: Lomb-Scargle periodogram of the *TESS* light curve, clearly showing the binary orbital period but with no evidence for any other periodicities. The orange dashed line shows the 1% false alarm probability. Bottom panel: Phase-folded light curve (blue) and sine model fit (orange), repeated twice for clarity. The residuals are shown as an O-C calculation.

$0.0183 \pm 0.0005$  mag for the 2018 February 01 (LDLC01010) COS spectrum and  $T_{\text{eff}} = 25162^{+19}_{-20}$  K,  $\log g = 7.564 \pm 0.005$  dex, and  $E(B - V) = 0.023 \pm 0.0005$  mag for the 2018 July 22 (LDLC51010) COS spectrum. We computed the mean and standard deviation using the two estimates of the parameters from the fits which account for systematic errors. These best-fit values are quoted in 1. Using the measured  $T_{\text{eff}}$  and  $\log g$  the mass and radius of the white dwarf can be computed using the mass-radius relation described above. For this purpose, we generated two samples containing 10000 data-points, one for the effective temperature and one for the surface gravity (both with normal distributions of  $T_{\text{eff}} = 25203 \pm 42$  K and  $\log g = 7.58 \pm 0.02$  dex, respectively; see Table 1). We computed the mass-radius relation on these distributions resulting in two normal distributions for the mass and radius described by

**Table 1.** Characteristics of the CC Cet system. References: 1. This work; 2. Gaia Collaboration et al. (2018); 3. Saffer et al. (1993); 4. Tappert et al. (2007) ✓

$T_{\text{eff}}$ (K)	$25203 \pm 42$	Ref: 1
$\log g$ ( $\text{cm s}^{-2}$ )	$7.58 \pm 0.02$	1
$E(B - V)$ (mag)	$0.021 \pm 0.002$	1
White dwarf Mass ( $M_{\odot}$ )	$0.441 \pm 0.008$	1
White dwarf Radius ( $R_{\odot}$ )	$0.0179 \pm 0.0003$	1
Parallax (mas)	$8.2381 \pm 0.0758$	2
Distance (pc)	$121.4 \pm 1.1$	1
Magnetic field strength (kG)	600–700	1
$v \sin i$ ( $\text{km s}^{-1}$ )	$\sim 40$	1
Secondary Mass ( $M_{\odot}$ )	$0.18 \pm 0.05$	3
Secondary Spectral Type	M4.5–5	3, 4
Orbital period ( <i>TESS</i> , h)	$6.8818 \pm 0.00045$	1
Ephemeris ( <i>TESS</i> , TJD)	$2459157.14821 \pm 0.00051$	1

$M_{\text{wd}} = 0.441 \pm 0.008 M_{\odot}$  and  $R_{\text{wd}} = 0.0179 \pm 0.0003 R_{\odot}$ , respectively (Table 1).

### 3.2 Spectral lines in the COS spectra of CC Cet

Figure 1 shows the COS G130M spectrum of CC Cet. The spectrum is typical of white dwarfs in this temperature range (Koester et al. 2014): dominated by the broad H I 1215.67 Å Lyman  $\alpha$  line, along with a mixture of shows a mixture of narrow and deep interstellar lines and broader, shallower photospheric lines. We detect no contribution from emission lines produced by the M dwarf, which is unsurprising given that the lack of flares in the *TESS* light curve indicates that the M dwarf is relatively inactive.

The interstellar lines are invariably due to resonance lines of neutral or singly-ionised abundant elements such as C II, N I, O I, Si II, and S II. Because the observed interstellar lines arise only from the lowest ground state level, it can sometimes happen that in a multiplet of resonance lines which is also present in the photospheric spectrum, only some of the lines of the multiplet are contaminated by interstellar scattering. This allows the photospheric lines to be reliably modelled without contamination from the interstellar lines.

The strongest photospheric lines present in the COS spectrum of CC Cet are primarily due to C III (six lines of UV multiplet (4) at 1175 Å), Si III (six lines of UV multiplet (4) between 1294 and 1303 Å), and Si IV (two lines of UV multiplet (1) at 1393 and 1402 Å). There are also two blended photospheric lines of Si II from UV multiplet (4) at 1265 Å.

### 3.3 Magnetic field

#### 3.3.1 Discovery of field

Closer examination of the photospheric lines reveals that they differ significantly from those in similar COS spectra. In particular, the resonance line of Si II at 1264.738 Å (which is slightly blended with a much weaker line in the same multiplet, but not blended with an interstellar line because it arises from a state a few hundred  $\text{cm}^{-1}$  above ground) shows a clear triplet structure composed of three very similar components separated by about 0.5 Å. The structure is strongly reminiscent of the appearance of the normal Zeeman triplet produced in many spectral lines by a magnetic field of tens or



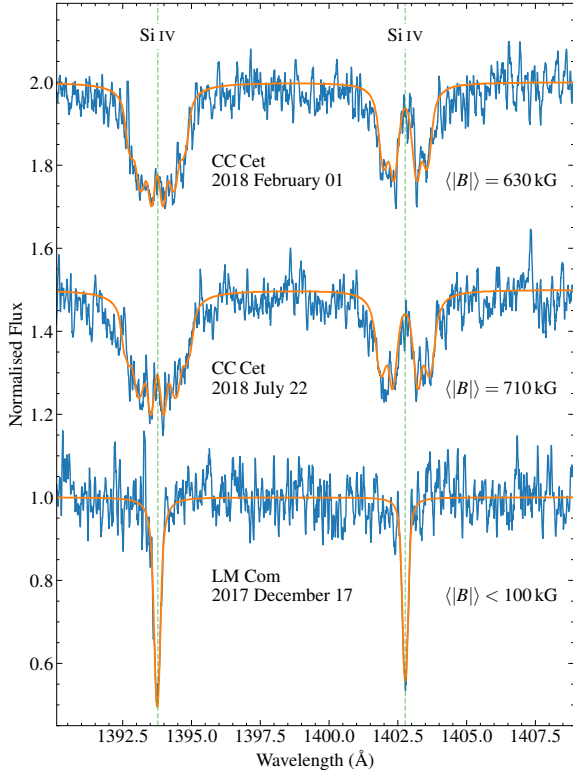


**Figure 3.** Silicon Si IV lines in the two *HST/COS* spectra of CC Cet, and one spectrum of LM Com, another PCEB with a similar  $T_{\text{eff}}$  and  $\log g$ . The difference between the Zeeman split lines in CC Cet and the non-magnetic LM Com is readily apparent. Orange line shows the best-fit magnetic model to the lines, and the dashed vertical lines show the rest wavelengths. The date and best-fit mean field modulus are given under each spectrum.

hundreds of kiloGauss (kG). The appearance of this feature strongly suggests that CC Cet has a magnetic field.

Furthermore, although the other strong photospheric lines do not show such obvious Zeeman splitting, they all look rather peculiar. The C III lines at 1175 Å show only three strong lines instead of the usual five. The usual six strong lines of Si III around 1300 Å appear as about 15 slightly weaker lines in the same length interval. The two Si IV lines at about 1400 Å, which normally show very similar Lorentzian profiles, instead are quite broad and different from one another. As we shall show below, these effects can be produced by a field of hundreds of kG.

### 3.3.2 Qualitative analysis of field

To obtain further information about the magnetic field which appears to be present in CC Cet, we start by estimating the mean field modulus  $\langle |B| \rangle$ , the value of the local field strength  $|B|$  averaged over the hemisphere visible at the time of observation. The observed splitting of the Si II  $\lambda 1264$  line is about 0.5 Å between each of the  $\sigma$  components and the central  $\pi$  component. This value may be used with the standard equation for the  $\pi - \sigma$  separation  $\Delta\lambda_Z$  due to the normal Zeeman effect for an initial field strength estimate:

$$\Delta\lambda_Z() = 4.67 \cdot 10^{-13} z \lambda_0^2 B, \quad (2)$$

where  $\lambda_0$  is the unperturbed wavelength of the line, wavelengths are measured in Å units,  $z = 1.43$  is the mean Landé factor of this

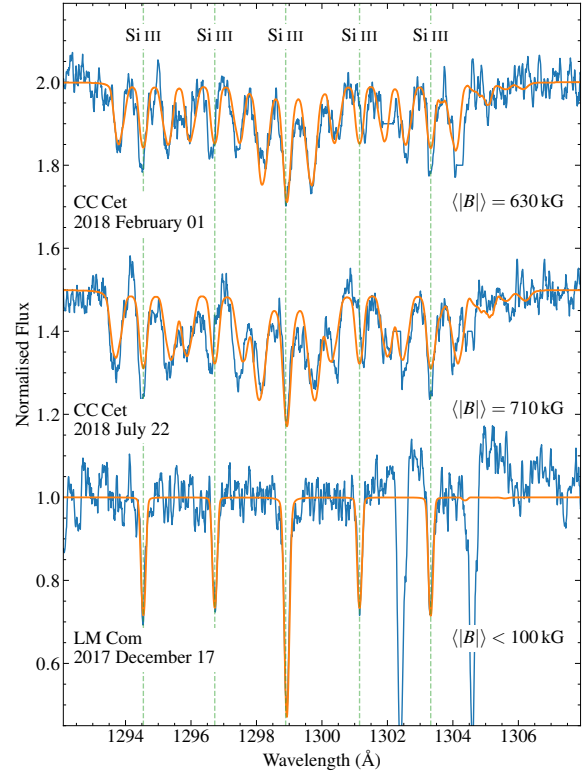


**Figure 4.** As Figure 3 but for Si III lines around 1300 Å. The deep unmarked absorption features in the LM Com spectrum are interstellar O I lines that have been removed from the spectrum of CC Cet. Note that each line in LM Com is replaced in the spectrum of CC Cet by a Zeeman triplet.

line, and  $B$  is the magnetic field strength in Gauss ( $10^4 \text{ G} = 1 \text{ Tesla}$ ). Applying this equation to the Si II line we deduce the presence of a field of  $B \sim 500 \text{ kG}$ .

A field of this strength is well within the regime of normal Zeeman splitting for transitions between two isolated atomic levels. However, for some of the multiplets of the light elements observed in CC Cet, the spacing between fine-structure levels of single LS terms is small enough that the level splitting by the Zeeman effect in a field of hundreds of kG is comparable to the unperturbed term level separation. Alternatively, one can say that the Zeeman splitting is so large that some of the outer Zeeman components approach or cross neighbouring lines of the multiplet. In this case, it is no longer correct to use the usual Zeeman splitting theory appropriate for lines formed between isolated levels. Instead, the magnetic field effect must be considered together with the fine structure splitting of the term. This case is known as the partial Paschen-Back effect, and we will discuss it below when we come to this situation.

### 3.3.3 Simple dipolar magnetic field models

Ideally, we would aim to obtain a low resolution map or model of the global structure of the magnetic field over the whole surface of CC Cet. In principle this is possible if a series of polarised spectra are obtained through the rotation period of the star, and these are modelled collectively. However, we have only two spectra, both of rather low  $S/N$ , without polarisation information. The stellar rotation period is fast (see below) but unknown, so the net phases of the observations are unknown.

The magnetic spectrum synthesis code used for this modelling was the code ZEEMAN.F (Landstreet 1988), which performs a forward line profile computation starting from a specified stellar atmosphere model, a specified magnetic configuration over the entire stellar surface, relevant geometric parameters such as the inclination  $i$  of the rotation axis and a range of projected rotation velocities, an abundance table for relevant elements, and a specified wavelength window and line list. The code computes the expected emergent Stokes parameters  $I$  (essentially the flux, normalised to the continuum for convenience, including emergent spectral line profiles), and the polarisation Stokes parameters  $Q$  and  $U$  (linear polarisation), and  $V$  (circular polarisation). The output flux and polarisation profiles can then be compared to the observed spectra. One or more parameters (such as the abundance of a specific chemical element) can be iterated by the code to improve the agreement between computed and observed spectra.

Because of the limited data available for CC Cet we cannot fully constrain even a very simple magnetic model such as a dipole field. Instead, we aimed to find a set of parameters that yield satisfactory fits to the lines in the modelled regions, and extract some general field properties from such models, such as a reasonably well-defined value of  $\langle |B| \rangle$ , information about the extent to which different spectral lines provide concordant estimates, and possibly an estimate of  $v \sin i$ . For this modelling we restricted the field structure to a dipole, or a dipole plus a weak opposing octupole that has the effect of reducing the range of local  $B$  variations over the surface.

### 3.3.4 Si IV UV multiplet (1)

Figure 3 shows the Si IV lines near 1400 Å, which can be fit reasonably well with a variety of simple dipole models. The two lines of this multiplet share a common lower level, and the two upper states are separated by about 460 cm<sup>-1</sup>, so that the lines are separated by about 9 Å, much more than the typical Zeeman splitting at 500 kG. Their splitting is thus accurately described by the normal Zeeman theory, and correctly computed by ZEEMAN.F. A typical fit of the lines in the spectral window around 1400 Å is shown in Figure 3. The strange spectral line profiles of the two Si IV lines in this window are easily understood as the effect of rather different Zeeman splitting patterns of the two lines. The line at 1402 Å comes from a  $^2S_{1/2}$  to  $^2P_{1/2}$  transition, whose Zeeman splitting pattern has the two  $\pi$  components almost as far apart as the two  $\sigma$  components, and thus forms effectively a Zeeman doublet, with almost no absorption at the unperturbed line centre because there are no regions of field near 0 kG. In contrast, the six Zeeman components of the 1393 Å  $^2S_{1/2}$  to  $^2P_{3/2}$  transition are pretty uniformly spaced through the profile, with the most displaced and weakest  $\sigma$  components at the outer edges of the line profile. This splitting pattern leads to a roughly U-shaped overall profile. (Many simple LS-coupling Zeeman splitting patterns are shown schematically by Condon & Shortley 1935, Fig. 46.) This region can be fit well with a wide variety of magnetic model parameters, provided that the mean field modulus is about 630 kG (for spectrum 01) or 710 kG (spectrum 02). The abundance of Si relative to H,  $\epsilon_{\text{Si}} = \log(n_{\text{Si}}/n_{\text{H}})$ , is found to be about  $-5.6 \pm 0.1$ .

### 3.3.5 Si III UV multiplet (4) and $v \sin i$

A second window that can be modelled fairly well in the Zeeman approximation is the set of six low excitation lines of Si III between

1294 and 1303 Å. These lines arise from transitions between two  $^3P$  terms, and a peculiarity of LS coupling leads to magnetically perturbed levels of non-zero  $J$  having identical level separation with anomalous Landé  $g$ -factor 1.5 (i.e. the level separation is 1.5 times larger than in the normal Zeeman separation). This splitting pattern replaces each of the single lines of the sextuplet by three lines, and the strength of the field just happens to be a value for which the added  $\sigma$  components of the lines fall in between the central  $\pi$  components (which lie approximately at the wavelengths of the magnetically unperturbed sextet), and replace the original lines with a forest of about 15 distinct lines, approximately equally spaced (two lines of the original sextet almost coincide in wavelength). This effect is shown in Fig 4, where the original lines of the multiplet (now  $\pi$  components, have been marked).

In this set of lines, the separation between  $\sigma$  and  $\pi$  Zeeman components is comparable to the separation between lines of the sextet. Correspondingly, the magnetic splitting of some of the individual multiplet levels is comparable to the separations between both the lower and the upper term levels. In this situation the simple weak-field Zeeman splitting is no longer an accurate description; instead the splitting is making the transition to Paschen-Back splitting, and both magnetic and fine structure splitting should be computed together. Partial Paschen-Back splitting is not built into ZEEMAN.F, so our computations assume that the usual expression for the anomalous Zeeman effect apply. This approximation meant that the simple magnetic models that fit the Si IV lines at 1400 Å did not produce good fits to the other strong lines.

### 3.3.6 Partial Paschen-Back splitting

The partial Paschen-Back effect, and how to compute its effects on the lines of a multiplet, is discussed extensively by Landi Degl'Innocenti & Landolfi (2004, Chapter XXX). We were fortunate to obtain a FORTRAN program, GIDI.F, from Dr Stefano Baguolo, that we believe was originally written by Prof degl'Innocenti. This program solves the problem of the combined effect of magnetic and fine structure splitting of a single multiplet that is described by LS coupling. This approximation is appropriate for most light elements, including C and Si. A calculation of the splitting of the  $3s3p\ ^3P^o - 3p^2\ ^3P$  transition that leads to the sextet of lines at 1300 Å indicates that the most significant effect of the partial Paschen-Back effect is to shift the  $\pi$  components of the 1296.72 and 1301.15 by about 0.12 Å at 600 kG, to the blue for the 1296 line and to the red for the 1301 line. Exactly this effect is clearly observed in the discrepancy between our fit using only conventional Zeeman splitting, and the observations shown in Fig. 4. Otherwise, the simple Zeeman effect computation of ZEEMAN.F provides a reasonable fit, and allows us to refine the strength of the field observed.

The value of the Si abundance can also be determined from the model for the Si III window. We find values of  $\epsilon_{\text{Si}} \approx -6.1$  to  $-6.3$ . Note that this abundance is about a factor of three lower than the abundance level deduced from the Si IV lines. The origin of this difference is not known, but may represent an overabundance of the Si IV/Si III ratio produced by non-LTE effects that cannot be predicted by our LTE code, an effect of vertical stratification (Koester et al. 2014), or perhaps an effect of non-uniform distribution of Si over the stellar surface, as is found on upper main sequence magnetic stars.

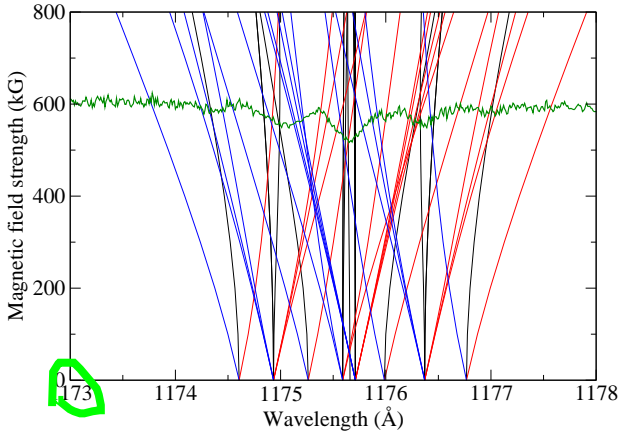


**Figure 5.** "Spaghetti diagram" showing wavelengths of individual magnetic subcomponents of the C III sextet at 1175 Å as a function of magnetic field strength, computed as a partial Paschen-Back case. Subcomponents are colour-coded as blue  $\sigma$  (blue),  $\pi$  (black), and red  $\sigma$  (red). COS flux spectrum (green) plotted with continuum set at about 600 kG to show how main line features correspond with clustering of magnetic subcomponents.

### 3.3.7 Other UV spectral lines

The Si II line at 1265 Å is actually one of three resonance lines formed by the  $3p^2P^o$  to  $3d^2D$ , UV multiplet (4). Two of the three lines nearly coincide at 1264.730 (strong) and 1265.023 Å (weak). This pair, not blended with interstellar contamination, show the magnetic splitting that led to the discovery of the field of CC Cet. The effect of the partial Paschen-Back effect is to shift all the components of the weaker line towards the blue, and those of the stronger line towards the red, so that radial velocities measured with the  $\pi$  or  $\sigma$  components of the stronger line in a field near 600 kG will be systematically red shifted from radial velocities measured with lines unaffected by the partial Paschen-Back effect, such as those from the Si IV doublet at 1400 Å. However, the normal Zeeman effect is not a bad approximation at 600 kG, and models of this feature with ZEEMAN.F fit reasonably well assuming a field structure with  $\langle |B| \rangle \approx 550$  kG.

As discussed above, because the partial Paschen-Back splitting of lines is not implemented in our line synthesis code, we cannot produce an accurate model of the C III multiplet (4) at 1175 Å. However, using GIDLF, we have computed the variation of the line splitting as a function magnetic field strength up to 800 kG. Below about 200 kG, the splitting of the individual lines of the multiplet follows closely the prediction of the Zeeman theory. However, by about 600 kG, the splitting is converging on the Paschen-Back limit. In fact, the computed splitting at 600 kG quite closely resembles the observed multiplet, with five groups of line components whose centroids coincide almost exactly with the positions of the observed components, and that agree qualitatively with the relative strengths of those components (Fig. 5).

### 3.3.8 H in the optical spectrum

Two UVES optical spectra of CC Cet were obtained for the SPY program (Napiwotzki et al. 2020; Koester et al. 2009) and are avail-

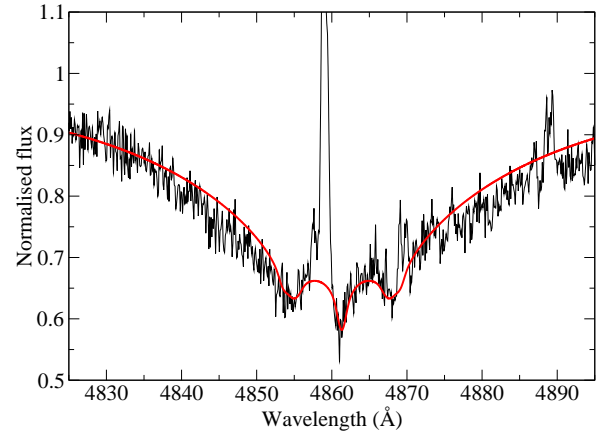


**Figure 6.** H $\beta$  from UVES spectrum of CC Cet (black) with overplotted fit to line core assuming approximately dipolar magnetic field with  $\langle |B| \rangle = 620$  kG. Zeeman triplet is obvious in spite of strong emission line from M dwarf secondary star.

able from the ESO Archive. These data cover the entire Balmer spectrum in the visible with resolving power of about 20 000 and SNR of roughly 15–20. Balmer lines H $\alpha$  to H $\epsilon$  are clearly visible in the spectra. We have examined the cores of these lines for evidence of the magnetic field of CC Cet. Because of the low SNR and the presence of emission lines from the M dwarf companion, especially strong in H $\alpha$  and H $\beta$ , the magnetic splitting of the Balmer lines by the 700 kG field is not immediately obvious. However, if we smooth the UVES spectra slightly and shift the two spectra to the same radial velocity framework, the superposed H $\beta$  lines reveal fairly clear Zeeman triplet structure, with splitting that agrees closely with that expected from the UV lines. One spectrum with a model fit is shown in Figure 6.

### 3.3.9 Rotation velocity

A remarkable feature of both the Si III 1300 Å and Si IV 1400 Å lines is that, if the rotational velocity of the white dwarf is taken to be close to 0 km s $^{-1}$ , the computed patterns have deep, narrow  $\pi$  components, especially in the 1393 Å line, which are not present in the observed profiles. The  $\pi$  components of each line are not broadened by a variation of values of the local magnetic field strength  $B$  over the visible hemisphere, so the broadening may instead be due to a rapid rotation of the white dwarf. Fitting the cleanest  $\pi$  components (not significantly broadened by a spread in local magnetic field values  $|B|$  over the visible hemisphere) showed clearly that it is necessary to assume  $v \sin i \approx 40 \pm 10$  km s $^{-1}$  to obtain the best fit to the observed  $\pi$  components.

However, CC Cet is part of a short-period binary system with an M4.5 main sequence star. The velocity semi-amplitude of the M dwarf is about 120 km s $^{-1}$  (Saffer et al. 1993). Because the white dwarf has a mass very close to twice that of the M dwarf, its velocity semi-amplitude is about 60 km s $^{-1}$ , with the full range being covered in about 3.5 h. During a single 0.5 h COS exposure, the radial velocity of the white dwarf could therefore change by as much as 25 km s $^{-1}$ . This effect is not included in the explicit velocity broadening of the computed spectrum, but together with the resolving

power and the small wavelength spread due to the partial Paschen-Back effect could account for a maximum line broadening of about  $35 \text{ km s}^{-1}$  FWHM. The observed  $\pi$  components of this multiplet are about  $60 \text{ km s}^{-1}$  in FWHM in both of the COS spectra. Thus although the deduced value of  $v \sin i$  may be slightly overestimated, it is very unlikely that  $v \sin i$  is actually much smaller than  $40 \text{ km s}^{-1}$ , implying that the white dwarf could have a rotation period of the order of  $10^3 \text{ s}$ .

The spin period/orbital period ratio of CC Cet is therefore  $\approx 0.05$ , consistent with the bulk of the intermediate polars with spin and orbital period measurements (Bernardini et al. 2017). The difference in the line profiles between the two spectra indicate that the magnetic field axis is offset from the rotation axis and/or the metals are not evenly distributed across the white dwarf surface, so it may be possible to measure the rotation period from high cadence, high signal photometry or spectroscopy. No rotation signal is detected in the *TESS* light curve, although the red *TESS* bandpass is dominated by the M dwarf and may not be sensitive to subtle flux variations from the white dwarf. We attempted to produce time-series spectroscopy from the COS data using the `costools splittag`<sup>4</sup> routine to split the time-tag files into 30 s bins, but the S/N became too low to reliably measure any periodic flux or absorption line variation.

[... which is comparable to the spin period of many IPs. We could measure  $v \sin i$  for the other PCEBs (needs a bit more work on the COS data to correct for orbital smearing, and make a histogram of  $v \sin i$ . Include the (few) measurements that are available for CVs (VW Hyl, U Gem)? For the non-magnetic systems, we probably don't resolve  $v \sin i$  in the COS spectroscopy... so we only get an upper limit. There is one non-magnetic PCEB that contains a pulsating white dwarf, and JJ determined a spin period of 2.49h. <https://ui.adsabs.harvard.edu/abs/2015MNRAS.451.1701H/abstract>. With a radius of  $0.013 R_{\odot}$ , that would correspond to a rotational broadening of  $\approx 6 \text{ km/s}$ ... which we would not resolve with COS.]

### 3.3.10 Results of the magnetic analysis

The following conclusions can be drawn from our magnetic modelling efforts. (1) CC Cet has  $v \sin i \approx 40 \text{ km s}^{-1}$ , and therefore has a rotation period of about 1000 s or less. The rotation of the WD is very probably not synchronised with the orbital motion. (2) The typical value of  $\langle |B| \rangle$  on CC Cet is about 600–700 kG. This value may be modestly different during the two COS observations. The deduced value of the field appears to generally consistent with the splitting of all photospheric lines in the spectrum, although some observed lines (such as the sextet of lines of C III at  $1175 \text{ \AA}$ ), are split by the partial Paschen-Back effect in ways that our modelling code cannot reproduce accurately. (3) It appears, from the fact that the  $\sigma$  components of the Si III sextet are hardly broader than the  $\pi$  components, that the field is fairly homogeneous in local strength  $|B|$  over the visible hemisphere; the local field strength probably varies mostly by less than  $\pm 100 \text{ kG}$  in magnitude. (4) Correspondingly, the fact that the centre of the  $1402 \text{ \AA}$  line reaches almost to the continuum shows that there are no important regions of field strength close to zero on the visible surface. These facts are consistent with, but do not strongly require, a roughly dipole-like field, similar to those found in some other low field magnetic WDs that have been modelled in detail (e.g. WD 2047+372: see Landstreet et al. 2017).

<sup>4</sup> <https://costools.readthedocs.io/en/latest/index.html>

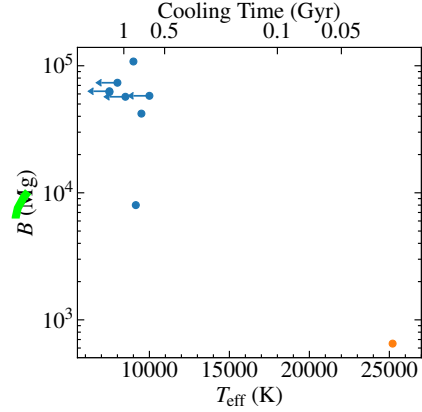


**Figure 7.** Temperatures and magnetic field strengths of known magnetic white dwarfs in PCEBs compiled by Ferrario et al. (2015) (blue) compared with CC Cet (orange). An approximate cooling time scale is given on the top axis. CC Cet is clearly an extreme outlier in both  $T_{\text{eff}}$  and  $B$ .

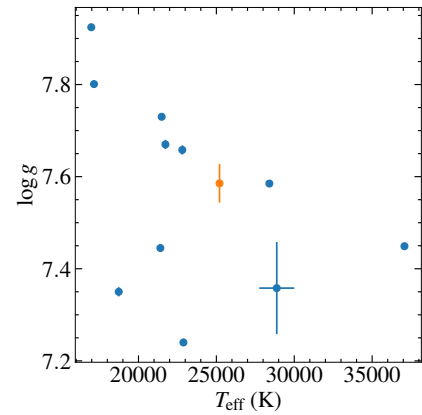


**Figure 8.** Atmospheric parameters of the white dwarfs in PCEBs observed with *HST*/COS, demonstrating that CC Cet (orange) is not an outlier in either  $T_{\text{eff}}$  or  $\log g$ .

## 4 DISCUSSION

### 4.1 CC Cet in context

Figure 7 compares CC Cet effective temperatures and magnetic field strengths of the magnetic PCEBs compiled by (Ferrario et al. 2015). CC Cet is clearly an extreme outlier, being both much hotter and (therefore younger) than the rest of the sample and having a much weaker magnetic field strength, even in comparison to the other confirmed pre-intermediate polar SDSS J030308.35+005444.1. CC Cet is an outlier by  $6\sigma$  and  $19\sigma$  in  $\log B$  and  $T_{\text{eff}}$  respectively. Invoking a common origin for the rare magnetic fields in PCEB white dwarfs would imply a large and thus far undetected population filling the parameter space in between CC Cet and the rest of the sample. We speculate that it is instead more likely that two formation pathways exist, one that can induce weak magnetic fields during or soon after the common envelope phase, as in CC Cet, and another that induces stronger fields as the systems age to produce the pre-polar population.

Along with CC Cet, program 15189 observed 9 other PCEBs containing a white dwarf and an M dwarf with the same COS setup.



Archival COS spectra of three more PCEBs demonstrating metal absorption lines are also available. Although a full analysis of these observations will be left for a future publication, we can use them to estimate an occurrence rate for magnetic PCEBs. All 12 additional white dwarf spectra show metal absorption lines, with no detectable magnetic field ( $\langle |B| \rangle \lesssim 100$  kG). Although the PCEBs were selected for practicality of observation, rather than to provide an unbiased sample, a comparison of the white dwarf atmospheric parameters (Figure 8) demonstrates that CC Cet is typical of the sample. Using the `astropy.stats.binned_binom_proportion` function we calculate an occurrence rate of  $7.7^{+14}_{-2.5}$  per cent, where the uncertainties are the  $1\sigma$  confidence boundaries. This stands in stark contrast to the 0/1735 ( $< 0.11$  per cent) and 2/1200 ( $0.17^{+0.22}_{-0.05}$  per cent) rates found by Liebert et al. (2015) and (Silvestri et al. 2007) respectively. The reason for this discrepancy is unclear, as the detection of Zeeman splitting in the relatively low S/N, optical UVES spectrum of CC Cet challenges explanations based on the change in wavelength regimes and/or detection limits. It is possible that we simply got lucky.

## 4.2 Formation/evolution

### 4.2.1 Mass

Compilations of observed magnetic white dwarfs have consistently shown that they have a higher average mass than non-magnetic white dwarfs (Liebert 1988; Ferrario et al. 2005, 2020),  $\approx 0.8 M_{\odot}$  compared with  $\approx 0.6 M_{\odot}$ . The known CV population also has an average mass around  $\approx 0.8 M_{\odot}$  (Zorotovic et al. 2011), and only a handful of low-mass CV white dwarfs with likely helium core compositions are known (Yu et al. 2019; Beuermann et al. 2020). CV population models predict large numbers of low-mass white dwarfs, and the reasons for the non-detection of those systems in the real world are still debated (Schreiber et al. 2016). We find a mass of  $0.441 \pm 0.008 M_{\odot}$  for CC Cet, low in comparison to both the magnetic white dwarf and CV populations and indicating that it is a He-core white dwarf (Driebe et al. 1998; Althaus et al. 2013). Magnetic white dwarfs with low mass are not unheard of: Bagnulo & Landstreet (2019) identify four magnetic, H atmosphere white dwarfs with masses  $\lesssim 0.5 M_{\odot}$  per cent of the total. Nevertheless, it may be that the non-detection of similar objects to CC Cet is due to inefficient formation of magnetic fields in low-mass white dwarfs, irrespective of their binarity.

### 4.2.2 Future of CC-Cet

The future of CC Cet was first modelled by Schreiber & Gänsicke (2003). They found that the companion will fill its Roche-lobe and start mass transfer onto the white dwarf, becoming a cataclysmic variable once the system have evolved down to an orbital period of  $P_{\text{orb}} \approx 2$  h in  $\approx 23$  Gyr.

Here we improve on those calculations using the state-of-the-art stellar evolution code Modules for Experiments in Stellar Astrophysics (MESA v.12778, Paxton et al. 2011, 2013, 2015, 2018, 2019). The standard model of evolution for CVs states that the orbital period is reduced via angular momentum losses driven by gravitational wave radiation (Paczynski 1967) and magnetic braking generated by the secondary (donor) star (Verbunt & Zwaan 1981; Rappaport et al. 1983; Mestel & Spruit 1987; Kawaler 1988; Andronov et al. 2003). However, if the system contains a magnetic white dwarf, the magnetic flux in open field lines responsible for magnetic braking is reduced, and therefore the magnetic braking of the secondary

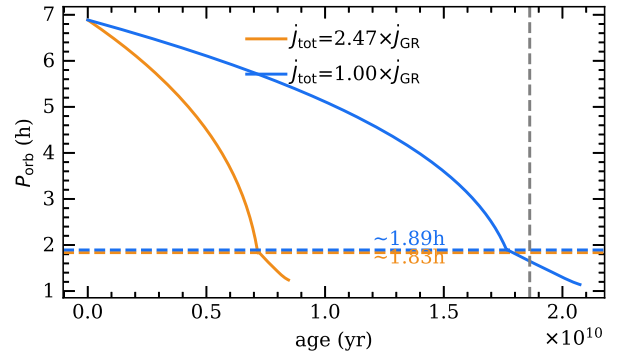


**Figure 9.** MESA simulations adopting angular momentum loss via gravitational wave radiation using the classical prescription (Paczynski 1967) and the calibrated version (Knigge et al. 2011, orange line). Our simulations show that CC Cet will become into a white dwarf accreting from its the low-mass main sequence companion (i.e. a cataclysmic variable) in the next 17.7 Gyr and 7.2 Gyr, for the classical and the calibrated versions of gravitational radiation, respectively. The vertical dashed line shows the calculations performed by Schreiber & Gänsicke (2003) using the classical prescription, which is slightly longer than in our simulations. The system will have an orbital period shorter than 2 hr when the accretion starts (dashed lines).

reduces significantly (Li et al. 1994; Li & Wickramasinghe 1998; Webbink & Wickramasinghe 2002). The magnetic braking is also thought to become very inefficient once the systems reach to orbital periods around  $\approx 3$  h, which could be the result of the donor becoming fully convective. The abruptly decrease of donor's magnetic braking causes the mass transfer to halt (and thus the detached systems sit in the commonly denominated period gap;  $\sim 2 - 3$  h). The subsequent evolution is driven mainly by angular momentum loss via gravitational radiation. With decreasing period the Roche lobe of the donor reduces, and at a period roughly of 2 h the donor once again overflows its Roche lobe, resuming mass transfer and exiting the period gap.

For our simulations we adopt an initial orbital period of 0.287 d and treat the white dwarf as a point source with a mass  $0.44 M_{\odot}$  (Table 1). We assumed that all the accreted mass onto the white dwarf is not retained (`MASS_TRANSFER_BETA` = 1.0) and adopted the  $M_{\text{donor}} = 0.18 \pm 0.05 M_{\odot}$  secondary mass from Saffer et al. (1993). The low mass of the main-sequence star indicates a fully convective star, therefore magnetic braking in CC Cet is inoperative and the reduction of CC Cet's orbit is driven only by the angular momentum loss via emission of gravitational waves. In our simulations we accounted for two prescriptions for the gravitational wave radiation: 1. the classical prescription dictated by Einstein's quadrupole formula (Paczynski 1967) and 2. the calibrated version, which reproduces the observed masses and radii of the donors in cataclysmic variables (Knigge et al. 2011). We stopped the simulations when the mass of the donor reached the brown dwarf mass limit (`STAR_MASS_MIN_LIMIT` =  $0.08 M_{\odot}$ ).

Our simulations show that the final fate of CC Cet is to become an intermediate polar. The system will start to transfer mass at a low rate of  $\approx 10^{-10.45} M_{\odot}/\text{yr}$  ( $\approx 10^{-10} M_{\odot}/\text{yr}$ ) in roughly the next 17.7 Gyr (7.2 Gyr) for the classical (calibrated) version of gravitational radiation. The system will have an orbital period lower than 2 h when the accretion starts (Figure 9). The accretion rate will slightly decrease while the system continues shrinking, until the mass of the donor reaches a mass of  $0.08 M_{\odot}$  at an orbital period of  $\approx 1.14$  h ( $\approx 1.24$  h).

Norton et al. (2004) modelled the magnetic moment of IPs given their measured spin period to orbital period ratios. Given that we know the magnetic moment of CC Cet ( $\mu_1 = BR^3 \approx 1.35 \times 10^{33} \text{ G cm}^{-3}$ ), we can use their Figure 2 to estimate the white dwarf spin period when it reaches the orbital period minimums calculated above. We find equilibrium spin periods of  $\approx 1.7 \text{ m}$  ( $\approx 1.9 \text{ m}$ ) for orbital periods of  $\approx 1.14 \text{ h}$  ( $\approx 1.24 \text{ h}$ ).

### 4.3 M dwarf wind

As mass-transfer by Roche lobe overflow has not yet begun in the CC Cet system, the origin of the metals in the white dwarf atmosphere is most likely the stellar wind of the M dwarf companion. Debes (2006) has demonstrated that such wind accreting systems can be used to quantify the wind mass-loss rates of M dwarfs, which is otherwise extremely difficult to measure (see Wood 2018 for a summary of the current state of the art). Debes (2006) assumed that the non-magnetic white dwarfs in their sample accreted via the Bondi-Hoyle process (Bondi & Hoyle 1944), where the white dwarf gathers a fraction of the stellar wind in proportion to the white dwarf's gravity. Webbink & Wickramasinghe (2005) demonstrated that for binaries containing white dwarfs with high (10s of MG, i.e. pre polars) magnetic fields, the energy density of the magnetic field is much stronger than that of the wind down to the surface of the secondary, and thus the white dwarf accretes all of the wind emitted. CC Cet is an intermediate case, where the magnetic field is not strong enough to accrete all of the wind but nevertheless gathers wind from a wider radius than the Bondi-Hoyle process. Following the model from Section 6 of Webbink & Wickramasinghe (2005), the wind will be accreted inside of a critical radius  $r_{\text{crit}}$  from the white dwarf where the energy density of the magnetic field exceeds that of the wind:

$$\frac{\left(B_0 \left(\frac{r_{\text{wd}}}{r_{\text{crit}}}\right)^3\right)^2}{8\pi} = u_0 \left(\frac{r_{\text{md}}}{a - r_{\text{crit}}}\right)^2 \quad (3)$$

Where  $B_0$  is the strength of the magnetic field at the white dwarf surface,  $u_0$  the energy density of the wind at the secondary surface,  $a$  the orbital separation, and  $r_{\text{wd}}$  and  $r_{\text{md}}$  the radii of the primary and secondary respectively. Taking the average of our two magnetic field measurements and adopting a secondary radius of  $r_{\text{md}} = 0.243 R_{\odot}$  from the latest version of the tables from Pecauf & Mamajek (2013)<sup>5</sup>, we numerically solve equation 3 to find a critical radius of  $\approx 1.2 R_{\odot}$ , 75 percent of the orbital radius and roughly twice the Bondi radius. Assuming (incorrectly, but close enough for our purposes) that the M dwarf emits wind uniformly in all directions, the accretion rate of wind siphoned onto the white dwarf  $\dot{M}_{\text{wd}}$  is:

$$\dot{M}_{\text{wd}} = \dot{M}_{\text{wind}} \left(\frac{r_{\text{crit}}}{a}\right)^2 \quad (4)$$

To calculate  $\dot{M}_{\text{wd}}$ , we take the average of our measured Si abundance and calculate an accretion rate assuming that the atmosphere is in accretion diffusion equilibrium (Koester 2010), taking the diffusion timescale from the Montreal White Dwarf Database<sup>6</sup>. We

then assumed that the wind has Solar abundances, so scaled the Si accretion rate to the total accretion rate via the Si mass fraction measured by Asplund et al. (2009), arriving at an accretion rate onto the white dwarf of  $\approx 7.3 \times 10^9 \text{ g cm}^{-1}$ . Via equation 4, we therefore infer a wind mass loss rate  $\dot{M}_{\text{wind}}$  of  $\approx 1.3 \times 10^{10} \text{ g cm}^{-1}$  or  $\approx 2 \times 10^{-16} M_{\odot} \text{ yr}^{-1}$ . Repeating the calculation with only Bondi-Hoyle accretion in effect results in an inferred wind rate approximately an order of magnitude higher.

## 5 CONCLUSIONS

We have detected a 600–700 kG magnetic field on the white dwarf component of the detected PCEB CC Cet. CC Cet is by far the youngest and has the weakest field of all such systems yet discovered, and is so distinct from the rest of the sample that the field likely has a different origin. The white dwarf is rapidly rotating and demonstrates subtle variations in the absorption lines between spectra. Future high-cadence, high signal spectroscopy in the ultraviolet or blue optical may be able to map out the magnetic field structure and the surface distribution of metals accreted from the M dwarf companion.

## ACKNOWLEDGEMENTS

BTG was supported by a Leverhulme Research Fellowship and the UK STFC grant ST/T000406/1.

Based on observations made with the NASA/ESA Hubble Space Telescope, obtained from the Data Archive at the Space Telescope Science Institute, which is operated by the Association of Universities for Research in Astronomy, Inc., under NASA contract NAS 5-26555. These observations are associated with program # 15189.

## REFERENCES

- Althaus L. G., Miller Bertolami M. M., Córscico A. H., 2013, *A&A*, **557**, A19
- Andronov N., Pinsonneault M., Sills A., 2003, *ApJ*, **582**, 358
- Angel J. R. P., Borra E. F., Landstreet J. D., 1981, *ApJS*, **45**, 457
- Asplund M., Grevesse N., Sauval A. J., Scott P., 2009, *ARA&A*, **47**, 481
- Bagnulo S., Landstreet J. D., 2019, *A&A*, **630**, A65
- Bell K. J., et al., 2019, arXiv e-prints, p. arXiv:1910.04180
- Belloni D., Schreiber M. R., 2020, *MNRAS*, **492**, 1523
- Bernardini F., de Martino D., Mukai K., Russell D. M., Falanga M., Masetti N., Ferrigno C., Israel G., 2017, *MNRAS*, **470**, 4815
- Beuermann K., Burwitz V., Reinsch K., Schwöpe A., Thomas H. C., 2020, *A&A*, **634**, A91
- Bondi H., Hoyle F., 1944, *MNRAS*, **104**, 273
- Braithwaite J., Spruit H. C., 2004, *Nat*, **431**, 819
- Briggs G. P., Ferrario L., Tout C. A., Wickramasinghe D. T., Hurley J. R., 2015, *MNRAS*, **447**, 1713
- Briggs G. P., Ferrario L., Tout C. A., Wickramasinghe D. T., 2018, *MNRAS*, **481**, 3604
- Condon E. U., Shortley G. H., 1935, The Theory of Atomic Spectra
- Debes J. H., 2006, *ApJ*, **652**, 636
- Dekker H., D’Odorico S., Kaufer A., Delabre B., Kotzlowski H., 2000, in Iye M., Moorwood A. F., eds, Society of Photo-Optical Instrumentation Engineers (SPIE) Conference Series Vol. 4008, Optical and IR Telescope Instrumentation and Detectors. pp 534–545
- Driebe T., Schoenberner D., Bloeker T., Herwig F., 1998, *A&A*, **339**, 123
- Feinstein A. D., et al., 2019, *PASP*, **131**, 094502

<sup>5</sup> [http://www.pas.rochester.edu/~emamajek/EEM\\_dwarf\\_UBVIJHK\\_colors\\_Teff.txt](http://www.pas.rochester.edu/~emamajek/EEM_dwarf_UBVIJHK_colors_Teff.txt)

<sup>6</sup> <http://www.montrealwhitedwarfdatabase.org/evolution.html>

Ferrario L., Wickramasinghe D., Liebert J., Williams K. A., 2005, *MNRAS*, **361**, 1131

Ferrario L., de Martino D., Gänsicke B. T., 2015, *Space Sci. Rev.*, **191**, 111

Ferrario L., Wickramasinghe D., Kawka A., 2020, *Advances in Space Research*, **66**, 1025

Fitzpatrick E. L., 1999, *PASP*, **111**, 63

Fontaine G., Brassard P., Bergeron P., 2001, *PASP*, **113**, 409

Foreman-Mackey D., Hogg D. W., Lang D., Goodman J., 2013, *PASP*, **125**, 306

Gaia Collaboration Brown A. G. A., Vallenari A., Prusti T., de Bruijne J. H. J., Babusiaux C., Bailer-Jones C. A. L., 2018, preprint, ([arXiv:1804.09365](https://arxiv.org/abs/1804.09365))

Green J. C., et al., 2012, *ApJ*, **744**, 20

Isern J., García-Berro E., Külebi B., Lorén-Aguilar P., 2017, *ApJ*, **836**, L28

Kawaler S. D., 1988, *ApJ*, **333**, 236

Kawka A., Vennes S., pp 879–885

Knigge C., Baraffe I., Patterson J., 2011, *ApJS*, **194**, 28

Koester D., 2010, *Memorie della Societa Astronomica Italiana*, **81**, 921

Koester D., Voss B., Napiwotzki R., Christlieb N., Homeier D., Lisker T., Reimers D., Heber U., 2009, *A&A*, **505**, 441

Koester D., Gänsicke B. T., Farihi J., 2014, *A&A*, **566**, A34

Landi Degl’Innocenti E., Landolfi M., 2004, *Polarization in Spectral Lines*. Vol. 307, [doi:10.1007/978-1-4020-2415-3](https://doi.org/10.1007/978-1-4020-2415-3),

Landstreet J. D., 1988, *ApJ*, **326**, 967

Landstreet J. D., Bagnulo S., Valyavin G., Valeev A. F., 2017, *A&A*, **607**, A92

Li J., Wickramasinghe D. T., 1998, *MNRAS*, **300**, 718

Li J. K., Wu K. W., Wickramasinghe D. T., 1994, *MNRAS*, **268**, 61

Liebert J., 1988, *PASP*, **100**, 1302

Liebert J., et al., 2005, *AJ*, **129**, 2376

Liebert J., Ferrario L., Wickramasinghe D. T., Smith P. S., 2015, *ApJ*, **804**, 93

Lightkurve Collaboration et al., 2018, *Lightkurve: Kepler and TESS time series analysis in Python*, *Astrophysics Source Code Library* (ascl:1812.013)

Lopes de Oliveira R., Bruch A., Rodrigues C. V., Oliveira A. S., Mukai K., 2020, *ApJ*, **898**, L40

Mestel L., Spruit H. C., 1987, *MNRAS*, **226**, 57

Napiwotzki R., et al., 2020, *A&A*, **638**, A131

Nebot Gómez-Morán A., et al., 2011, *A&A*, **536**, A43

Norton A. J., Wynn G. A., Somerscales R. V., 2004, *ApJ*, **614**, 349

Norton A. J., Butters O. W., Parker T. L., Wynn G. A., 2008, *ApJ*, **672**, 524

Paczynski B., 1967, *Acta Astron.*, **17**, 287

Paczynski B., Sienkiewicz R., 1981, *ApJ*, **248**, L27

Pala A. F., et al., 2020, *MNRAS*, **494**, 3799

Parsons S. G., Marsh T. R., Gänsicke B. T., Schreiber M. R., Bours M. C. P., Dhillon V. S., Littlefair S. P., 2013, *MNRAS*, **436**, 241

Paxton B., Bildsten L., Dotter A., Herwig F., Lesaffre P., Timmes F., 2011, *ApJS*, **192**, 3

Paxton B., et al., 2013, *ApJS*, **208**, 4

Paxton B., et al., 2015, *ApJS*, **220**, 15

Paxton B., et al., 2018, *ApJS*, **234**, 34

Paxton B., et al., 2019, *ApJS*, **243**, 10

Pecaut M. J., Mamajek E. E., 2013, *ApJS*, **208**, 9

Potter S. B., Buckley D. A. H., 2018, *MNRAS*, **473**, 4692

Rappaport S., Joss P. C., Verbunt F., 1983, *ApJ*, **275**, 713

Rebassa-Mansergas A., Gänsicke B. T., Schreiber M. R., Koester D., Rodríguez-Gil P., 2010, *MNRAS*, **402**, 620

Saffer R. A., Wade R. A., Liebert J., Green R. F., Sion E. M., Bechtold J., Foss D., Kidder K., 1993, *AJ*, **105**, 1945

Schmidt G. D., et al., 2005, *ApJ*, **630**, 1037

Schmidt G. D., Szkody P., Henden A., Anderson S. F., Lamb D. Q., Margon B., Schneider D. P., 2007, *ApJ*, **654**, 521

Schreiber M. R., Gänsicke B. T., 2003, *A&A*, **406**, 305

Schreiber M. R., Zorotovic M., Wijnen T. P. G., 2016, *MNRAS*, **455**, L16

Schwope A. D., Nebot Gómez-Morán A., Schreiber M. R., Gänsicke B. T., 2009, *A&A*, **500**, 867

Silvestri N. M., et al., 2007, *AJ*, **134**, 741

**Table 1.** Interstellar absorption lines identified in the COS spectrum of CC-Cet. These lines are narrower than the white dwarf’s photospheric absorption lines since they are not affected by the rotational broadening of the white dwarf.

ion	wavelength (Å; vacuum)
C II	1334.532, 1335.703
N I	1134.165, 1134.415, 1134.980, 1199.549, 1200.224, 1200.711
O II	1302.168
Si II	1190.416, 1193.289, 1260.421, 1304.372
Si III	1206.510
Si IV	1393.755, 1402.770
S II	1250.586, 1253.812, 1259.520

Sion E. M., Schaefer K. G., Bond H. E., Saffer R. A., Cheng F. H., 1998, *ApJ*, **496**, L29

Sion E. M., Bond H. E., Lindler D., Godon P., Wickramasinghe D., Ferrario L., Dupuis J., 2012, *ApJ*, **751**, 66

Somers M. W., Lockley J. J., Naylor T., Wood J. H., 1996, *MNRAS*, **280**, 1277

Tappert C., Gänsicke B. T., Schmidtobreick L., Mennickent R. E., Navarrete F. P., 2007, *A&A*, **475**, 575

Toonen S., Hollands M., Gänsicke B. T., Boekholt T., 2017, *A&A*, **602**, A16

Verbunt F., Zwaan C., 1981, *A&A*, **100**, L7

Webbink R. F., Wickramasinghe D. T., 2002, *MNRAS*, **335**, 1

Webbink R. F., Wickramasinghe D. T., 2005, in Hameury J. M., Lasota J. P., eds, *Astronomical Society of the Pacific Conference Series Vol. 330, The Astrophysics of Cataclysmic Variables and Related Objects*. p. 137

Wickramasinghe D. T., Tout C. A., Ferrario L., 2014, *MNRAS*, **437**, 675

Woltjer L., 1964, *ApJ*, **140**, 1309

Wood B. E., 2018, in *Journal of Physics Conference Series*. p. 012028 ([arXiv:1809.01109](https://arxiv.org/abs/1809.01109)), [doi:10.1088/1742-6596/1100/1/012028](https://doi.org/10.1088/1742-6596/1100/1/012028)

Yu Z., et al., 2019, *MNRAS*, **489**, 1023

Zorotovic M., Schreiber M. R., Gänsicke B. T., 2011, *A&A*, **536**, A42

This paper has been typeset from a  $\text{\LaTeX}$  file prepared by the author.